J. Fluid Mech. (2008), *vol.* 602, *pp.* 267–286.
doi:10.1017/S0022112008000815 Printed in the United Kingdom

Shock tube flows past partially opened diaphragms

PAOLO GAETANI[1], ALBERTO GUARDONE[2] AND GIACOMO PERSICO[1]

[1]Dipartimento di Energetica, Politecnico di Milano, Via La Masa 34, 20156 Milano, Italy
[2]Dipartimento di Ingegneria Aerospaziale, Politecnico di Milano, Via La Masa 34, 20156 Milano, Italy

(Received 12 July 2007 and in revised form 21 January 2008)

Unsteady compressible flows resulting from the incomplete burst of the shock tube diaphragm are investigated both experimentally and numerically for different initial pressure ratios and opening diameters. The intensity of the shock wave is found to be lower than that corresponding to a complete opening. A heuristic relation is proposed to compute the shock strength as a function of the relative area of the open portion of the diaphragm. Strong pressure oscillations past the shock front are also observed. These multi-dimensional disturbances are generated when the initially normal shock wave diffracts from the diaphragm edges and reflects on the shock tube walls, resulting in a complex unsteady flow field behind the leading shock wave. The limiting local frequency of the pressure oscillations is found to be very close to the ratio of acoustic wave speed in the perturbed region to the shock tube diameter. The power associated with these pressure oscillations decreases with increasing distance from the diaphragm since the diffracted and reflected shocks partially coalesce into a single normal shock front. A simple analytical model is devised to explain the reduction of the local frequency of the disturbances as the distance from the leading shock increases.

1. Introduction

The imperfect burst of a shock tube diaphragm results in multi-dimensional disturbances that can significantly modify the flow field predicted by the ideal one-dimensional theory (see e.g. Rothkopf & Low 1974; Hickman, Farrar & Kyser 1975). For example, the finite diaphragm opening time has long since been demonstrated to locally accelerate the shock wave to speeds higher than those predicted by the one-dimensional theory, in the case of the very strong shocks studied by White (1958), Alpher & White (1958) and Petrie-Repar & Jacobs (1998). Non-ideal behaviour in shock tubes, including the influence of the viscous boundary layer on the shock propagation (see Mirels 1963; Mirels & Mullen 1964) and high-temperature chemical effects (see e.g. Gaydon & Hurle 1963), has also been investigated in detail during the past century (see Glass & Sislian 1994 for a review).

A peculiar behaviour is observed in the case of shock tube experiments in which the propagating shock wave is very weak. Owing to the small pressure difference across the diaphragm and the low total pressure behind the shock, i.e. of the flow through the diaphragm section, a complete opening is seldom attained. Persico, Gaetani & Guardone (2005) investigated post-shock disturbances due to the imperfect burst of the shock tube diaphragm in connection with the dynamic calibration

of fast-response pressure probes. For the calibration procedure, a weak shock wave – with a pressure step of about 0.3 bar – was used as the input signal to determine the transfer function of the probe. Multi-dimensional disturbances caused by the partial rupture of the diaphragm were reported and discussed, resulting in both post-shock pressure oscillations (with amplitude as large as 10% of the shock strength) and in a significant reduction of the shock intensity (as much as 30% in nominal conditions). Departure from ideality is also clearly present in other shock tube facilities for probe calibration (see e.g. Ainsworth & Allen 1990; Gossweiler, Humm & Kupferschmied 1990; Paniagua & Dénos 2002). Fergason, Guardone & Argrow (2003) and Guardone (2007) reported similar figures for a dense gas shock tube experiment, where the partial opening of the shock tube diaphragm was observed owing to the small pressure difference across the diaphragm. Note that in this kind of experiment, the influence of the boundary layer behind the shock wave is usually negligible, shock waves being almost acoustic waves propagating in a still fluid (see e.g. Glass & Sislian 1994).

In the present paper, the multi-dimensional unsteady flow field resulting from the incomplete burst of the diaphragm is studied. Both experimental and numerical studies are carried out to investigate multi-dimensional disturbances close to the diaphragm location as well as significantly downstream of it, where measurements are usually performed.

This paper is structured as follows. In §2, the experimental set-up is briefly described. The diaphragm opening behaviour is studied by means of high-speed camera recordings. In §3, the flow field close to the diaphragm is studied by means of total pressure measurements along the tube axis and of numerical simulations. The latter are then used to provide an explanation of the origin of post-shock disturbances. In §4, the flow field far from the diaphragm section is analysed. In particular, in §4.1, the intensity of the leading shock wave is discussed. In §4.2, post-shock disturbances are studied. A time-frequency analysis is performed and a simple wave propagation model is also proposed to explain the evolution of the local frequency of the pressure oscillations. The amplitude of the pressure oscillations along the tube is measured and its dependence on the axial distance from the diaphragm and on the dimension of the diaphragm opened section is studied. A commentary on the results concludes the paper in §5.

2. Experimental set-up

The experimental investigations are carried out in a open-ended shock tube with circular cross-sectional area.g The shock tube has an internal diameter D of 80 mm and a thickness of 5 mm and it is made of Plexiglas to allow for continuous optical access. The tube is divided into two sections separated by the diaphragm: the closed 1500 mm long high-pressure section; and the low-pressure section, whose length is 5000 mm. The low-pressure section of the shock tube is open to the laboratory (ambient) pressure P_a. The shock tube length has been chosen to allow for a relatively long time span (about 7 ms at 3000 mm from the diaphragm) of constant flow between the passage of the shock wave and the arrival of the rarefaction wave that has been reflected from the closed end of the tube.

Total pressure signals along the tube axis are measured by means of a fast-response miniaturized pressure probe to provide high time-resolution and minimize probe intrusiveness. Off-axis measurements have not been performed because of the slight asymmetry in the diaphragm opening process, that would in turn lead to poor

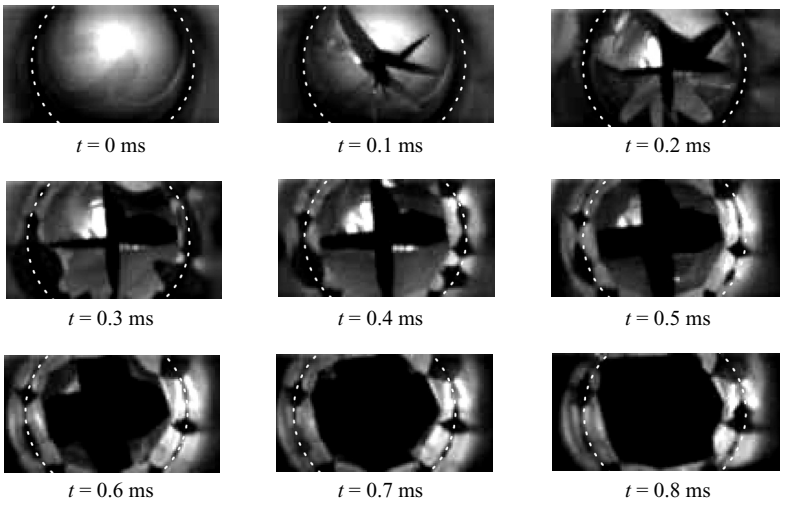

FIGURE 1. Diaphragm bursting process. An incomplete and nearly axisymmetric petalling of the plastic layer is attained after approximately 0.35 ms in nominal conditions. The sampling period is 0.02 ms.

repeatability away from the shock tube axis. The instrument consists of a piezoresistive pressure transducer (Kulite, model XCQ-062, FS = 1.72 bar) encapsulated in a brass tube with a diameter of 1.8 mm. The membrane of the transducer is flush mounted on the probe head; the frequency response of the probe without compensation is about 50 kHz (resonance frequency 175 kHz). Aerodynamic tests in a calibrated nozzle shows that the probe output is insensitive to flow angle fluctuations as large as $\pm 10^{\circ}$. At each measurement station, the probe is mounted on a linear traversing system to control the radial position of the probe with an accuracy of 0.01 mm. The probe output (± 80 mV-dc), is amplified by means of a broadband amplifier with a gain of about 150 over a 2 MHz band. A sampling frequency of 1 MHz is used, to be compared with the maximum measured frequency of 300 kHz. Additional details on the facility and instrumentation can be found in Persico *et al.* (2005).

2.1. *Shock tube diaphragm: design and operation*

In the present study, shock tube diaphragms have been manufactured using DCfix™ plastic, with a thickness of 0.1 mm. To simplify the experimental apparatus, no breaking systems were used to force the diaphragm open. Diaphragms are therefore designed to break automatically under a given pressure difference. To reduce the high deformation observed during the first experimental trials, the diaphragm has also been stiffened by adding four 0.05 mm thick triangular aluminium plates on the high-pressure side of the diaphragm.

The opening behaviour of the diaphragm determines the shape of the shock wave propagating towards the downstream section of the shock tube. Rothkopf & Low (1974) commented on the use of ductile materials in diaphragm manufacturing, resulting in a large deformation before the burst and an irregular petalling of the diaphragm. In the present study, the diaphragm bursting process has been studied by means of a high-speed camera (up to 50 000 frames per second). Despite the large initial deformation and the irregular petalling process, the envisaged diaphragm opening from the centre has been observed and the final opened section is approximately circular (figure 1). This suggests a shock evolution similar to that

Case	Measurements			
d/D -	N -	d (mm)	Δt_{open} (ms)	ΔP_{burst} (kPa)
0.7	49 (2)	54–58	∼0.35	∼122
0.6	25 (5)	46–50	∼0.28	∼105
0.5	19 (1)	38–42	∼0.21	∼84

TABLE 1. Classification of diaphragm behaviour from measurements. D and d are the diameters of the shock tube and of the opened portion of the diaphragm, respectively. N is the number of experimental runs resulting in an opened portion d included in the interval corresponding to each case (93 out of 145 runs are in the selected ranges). The diameter d is measured using a calibre and corrected to account for the plastic deformation of the diaphragm. The number within parentheses refers to additional measurements (8 out of 15 are in the selected ranges) performed with the high-speed camera to measure the opening time.

described by Hickman *et al.* (1975) and Petrie-Repar & Jacobs (1998), who reported the formation of a normal shock front sufficiently far from the diaphragm.

However, the diaphragm is found to open incompletely, with an opened diameter d smaller than 60 mm, namely, 75% of the internal tube diameter. This leaves an opened section of about 56% of the shock tube cross-sectional area. The opening times – measured as the elapsed time between the occurrence of the first crack in the diaphragm and the instant at which the final dimension is attained – are as high as $\Delta t_{open} = 0.35$ ms in nominal conditions ($d = 56$ mm). Note that larger opening sections (up to 90% of the internal diameter) and smaller opening times (0.07 ms) than those obtained here have been documented by Gossweiler *et al.* (1990), thanks to the adoption of pre-tensioned latex rubber membranes.

To investigate the effects of different opening diameters d on the shock tube flow, 1 mm thick metallic disks with circular orifice are added on the low-pressure side of the diaphragm. These additional plates allowed us to observe opening diameters ranging from 38 mm ($d/D = 0.5$ or 25% of the shock tube cross-sectional area) to 63 mm ($d/D = 0.8$ or 64% of the shock tube cross-sectional area), without the need to change the material or the manufacturing of the diaphragm. The opening time is found to increase with d, in accordance with the observations of Rothkopf & Low (1974). Experimental results are summarized in table 1, where experimental trials are gathered into three main cases, namely, $d/D = 0.5$, 0.6 and 0.7, the latter representing the nominal behaviour. The burst pressure difference ΔP_{burst} across the diaphragm is also found to decrease with d, see table 1, which in turns lead to a decrease of the expected shock strength. A dimensionless shock strength is used in the following to compare results from different test runs, see §4.1.

3. Flow field close to the diaphragm section

In this section the flow field features close to the diaphragm section, that is, for $x/D < 10$, are studied. To support the interpretation of the experimental results, a numerical model of the experimental set-up is devised.

The unsteady Euler solver of Guardone & Vigevano (2007) has been used, assuming negligible viscosity and thermal conductivity and an ideal polytropic, i.e. constant specific heats, thermodynamic description of the gas. In accordance with the observations from high-speed camera recordings, that revealed an axisymmetric

petalling of the diaphragm, the shock tube is described by an axisymmetric domain. To avoid the inclusion of a complex structural model of the diaphragm, the diaphragm dynamic is not taken into account by the numerical model. Numerical simulations are performed starting from the same initial conditions of the experiment and assuming that the diaphragm is partially, but instantaneously, opened. The consequences of this simplification are discussed in the following. Numerical results have been computed over an unstructured grid made of 122 667 triangles (63 976 nodes).

Numerical and experimental total pressure signals along the shock tube axis are reported in figure 2 for $d/D = 0.7$ and $P_4/P_1 = 1.9$, with P_1 and P_4 initial pressure in the driven and driver sections, respectively. The following dimensionless local and average shock strengths,

$$\pi(t) = \frac{P^t(t) - P_1}{\rho_1 c_1^2}, \qquad \Pi = \frac{\overline{P^t} - P_1}{\rho_1 c_1^2},$$

have been introduced, where $P^t(t)$ is the total pressure at the measurement point, $\overline{P^t}$ is the average post-shock total pressure and ρ_1 and c_1 are the density and the speed of sound in the unperturbed pre-shock state, respectively.

Relevant differences between experimental and numerical results are observed for about 0.35 ms after the arrival of the first signal, a time span that correlates to the measured diaphragm opening time (see table 1). The pressure levels of the experimental and numerical signals are very similar afterwards. Strong pressure oscillations are observed in the experiments. The local frequency of these oscillations is captured well by the numerical scheme, also when the mismatch between the amplitude of the pressure signals is more evident. The same behaviour is observed in the case $d/D = 0.6$ and $P_4/P_1 = 2.1$ (figure 3). In this case, relevant differences between the experiments and the simulations are limited to a time span of about 0.1 ms, to be compared with the observed diaphragm opening time of 0.28 ms, see table 1.

In all considered cases, numerical simulations are found to represent the experimental results along the axis of symmetry fairly well with the exception of an initial time interval which can be associated with the diaphragm dynamics, which is not modelled in the simulations.

The agreement between the numerical and experimental results allows us to use the former, which provide a more complete description of the instantaneous flow field, to explain the latter. For this purpose, a numerical simulation of the experiment close to the diaphragm section has been performed over an unstructured mesh made of 430 575 triangles (216 757 grid points) and considering a reduced shock tube length $L = 1.2$ m, or $L/D = 15$, centred at the diaphragm location. The (uniform) grid spacing at the diaphragm section is 0.1 mm, or $1.25 \times 10^{-4}\, D$. The pressure ratio P_4/P_1 is 2.068, which corresponds to the case $d/D = 0.6$ ($d = 48$ mm).

In figures 4–7, isobars and isopycnics of the simulated shock tube experiment are shown at times $t = 43$, 65, 195 and 293 μs, respectively. When the diaphragm is partially (but instantaneously) removed at time $t = 0$, a rarefaction wave moving towards the high-pressure section of the shock tube (the left-hand side of figure 4) is formed, together with a shock wave and a contact discontinuity moving towards the low-pressure section (right). Initially, these waves are planar and normal to the shock tube axis. At time $t = 43$ μs (figure 4), shortly after leaving the diaphragm section, the right-running shock wave partially diffracts to form an annular shock wave, indicated in figure 4 as *diffracted shock*. A portion of the initial shock wave remains

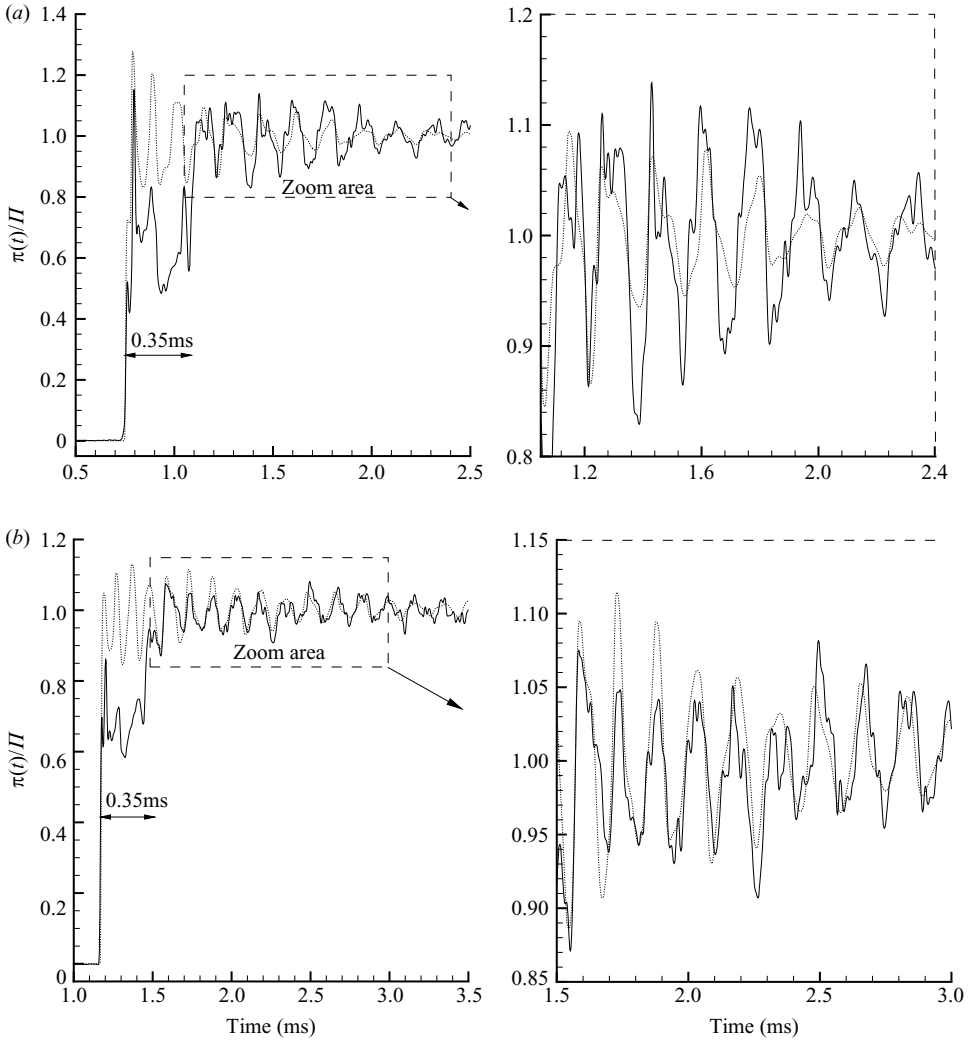

FIGURE 2. Total pressure measurements (—) past the partially opened shock tube diaphragm with $d/D = 0.7$ and $P_4/P_1 = 1.9$, against numerical simulations (···) with the axisymmetric Euler code. (*a*) Probe located in the first position (250 mm, about $3D$ downwind of the diaphragm). (*b*) Probe in the second position (450 mm, about $6D$ downwind of the diaphragm) along the shock tube driven section. The diaphragm opening time 350 μs is indicated in both the frames.

unchanged and moves as a planar shock, labelled as *normal shock*. The expansion at the diaphragm edge results in a *rarefaction wave* moving towards the shock tube axis. The rarefaction wave is faster than the leading normal shock and eventually collides with the shock itself. A similar wave system, with rarefaction instead of compression waves and vice versa, is formed in the high-pressure section. Flow separation occurs at the diaphragm edge. The slip surface from the diaphragm edge rolls up into an annular vortex. This is a well-known process that has already been observed in two-dimensional shock wave diffraction by Sun & Takayama (2003). At time $t = 65$ μs (figure 5), the diffracted portions of the initial shock and rarefaction waves are reflected by the tube walls. At later times, the rarefaction wave and the

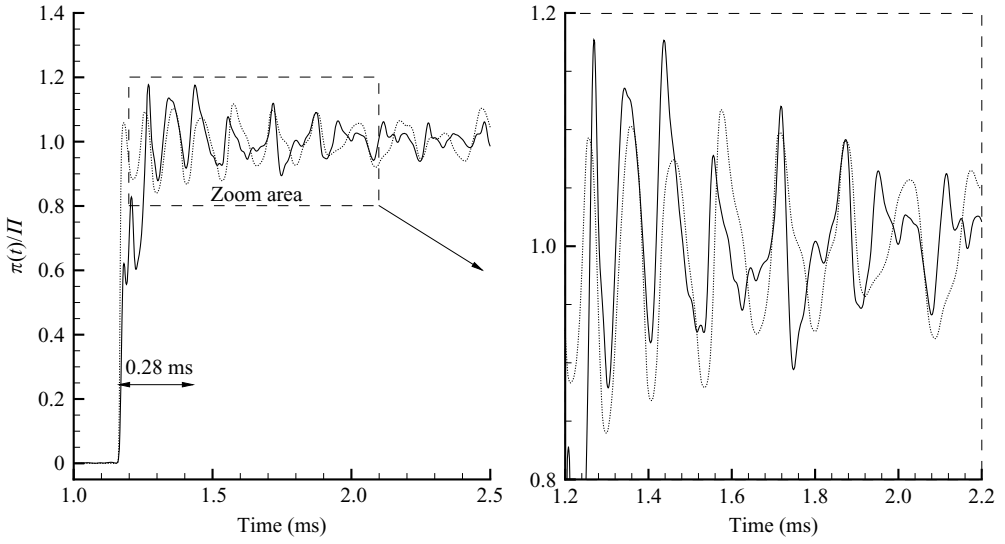

FIGURE 3. Total pressure measurements (—) past the partially opened shock tube diaphragm with $d/D = 0.6$ and $P_4/P_1 = 2.1$, against numerical simulations ($\cdots$). The probe is located at about $6D$ downwind of the diaphragm.

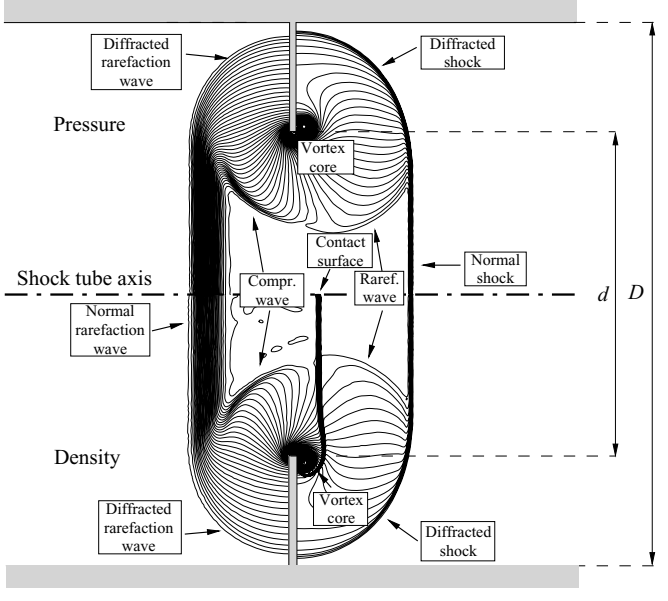

FIGURE 4. Isobars (top) and isopycnics (bottom) at time 43 μs for $d/D = 0.6$ and $P_4/P_1 = 2.068$.

compression wave centred at the diaphragm edge reflect at the tube axis. Moreover, the reflected shock interacts with the vortex and the contact surface, resulting in additional waves reflecting along the shock tube.

At time $t = 195$ μs (figure 6) the rarefaction wave, originally centred at the diaphragm edge and then reflected at the tube walls, collides with the leading shock resulting in a further reduction of the shock intensity. The wave propagation pattern

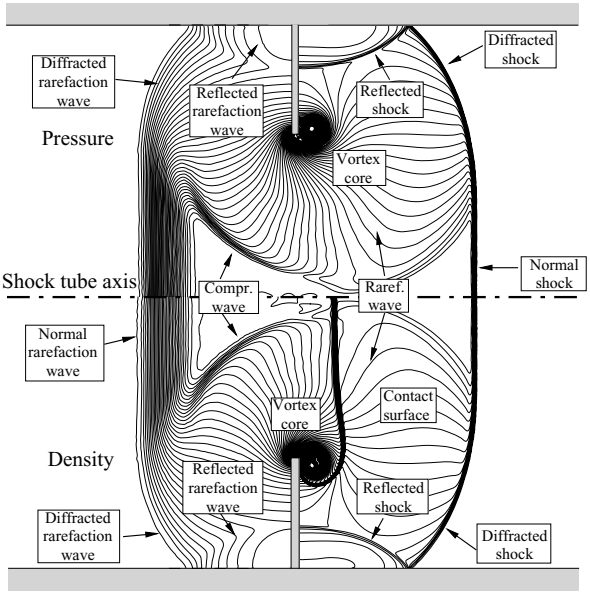

FIGURE 5. As figure 4, but for $t = 65$ μs.

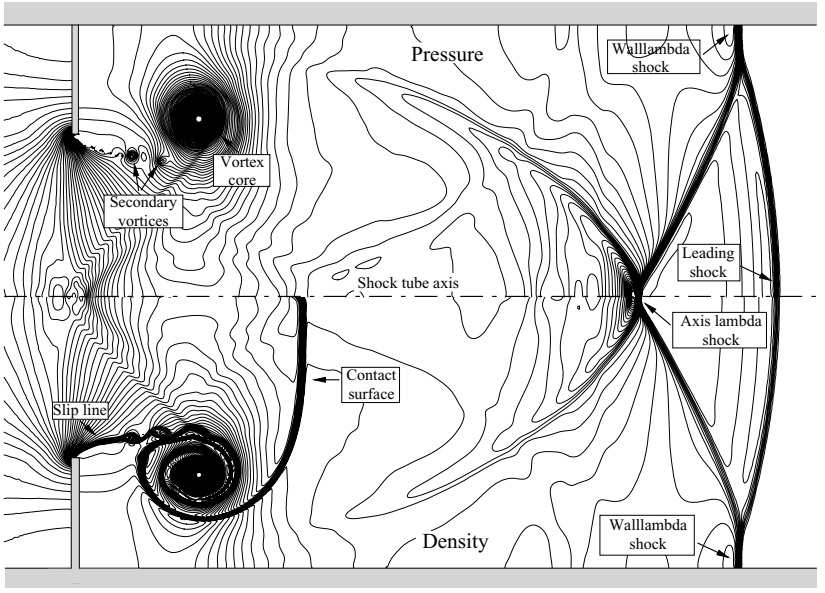

FIGURE 6. As figure 4, but for $t = 195$ μs.

is similar to that of a spherical wave, which would actually occur for $d/D \to 0$. In accordance with this observation, the angle between the shock and the wall increases in time, starting from 0° at the first reflection (cf. figure 4). The reflection pattern eventually evolves into a lambda shock, which is clearly observable in figure 6. The slip line undergoes a Kelvin–Helmholtz instability, which manifests itself as ripples

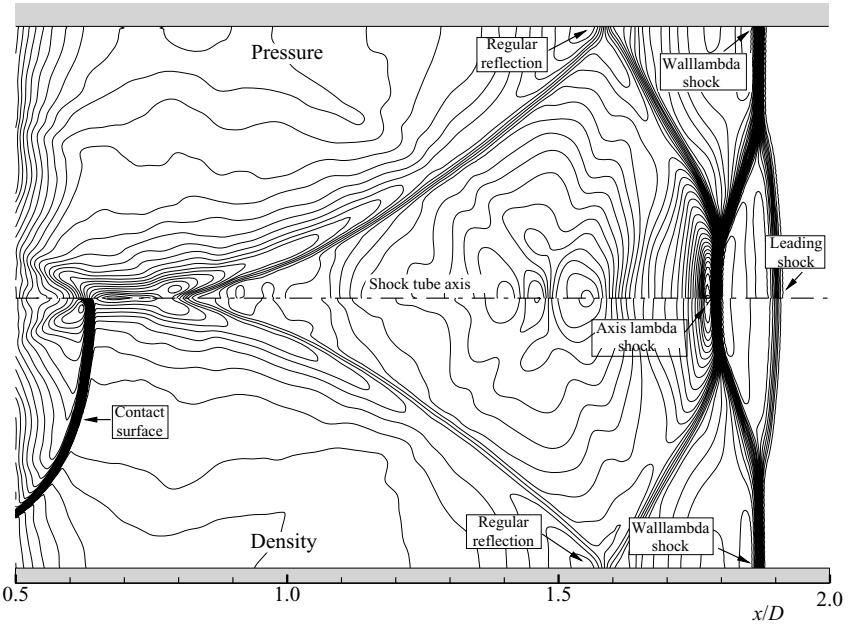

FIGURE 7. As figure 4, but for $t = 293$ μs.

in the isopycnics corresponding to secondary vortexes. These vortices are visible in the pressure field as local perturbations moving past the leading vortex. These small annular vortices are expected to trigger three-dimensional instabilities, eventually resulting in transition to turbulence. In this case, the velocity gradient across the slipstream would be significantly reduced by turbulent momentum transport. The occurrence of such a three-dimensional viscous flow field cannot be predicted under the axisymmetric (two-dimensional) inviscid approximation considered here. However, Sun & Takayama (2003) showed that an Euler computation is usually sufficient for the evaluation of both the intensity and the dynamic of the leading vortex.

In the high-pressure case considered by Petrie-Repar & Jacobs (1998), associated with a complete but not instantaneous opening of the diaphragm, the interaction of the shock front with the contact surface was shown to be very relevant. In that case, a small difference between the propagation speed of the shock and that of the contact surface was observed and the reflected portion of the shock was significantly weakened owing to the interaction with the contact surface. In the present case, the post-shock Mach number is about 0.15 and a complex shock wave reflection pattern is formed which is only weakly influenced by interaction with the contact surface. This observation allows us to explain why post-shock pressure oscillations are more intense in low-pressure shock tubes than in their high-pressure counterparts. The large difference between the propagation speed of the contact surface and that of acoustic waves can be appreciated by considering figure 7, where the flow field is shown at $t = 293$ μs. Moreover, two lambda shocks are clearly visible in figure 7. The first is located along the tube walls and results from the first reflection of the leading shock. The second lambda shock occurs at the axis of symmetry and originates from the focusing of the first reflected shock, a mechanism that has been studied in detail by Barkhudarov *et al.* (1991). The following reflections at the tube walls and at the axis are of the regular type. The results reported in figures 4–7 allow us to explain

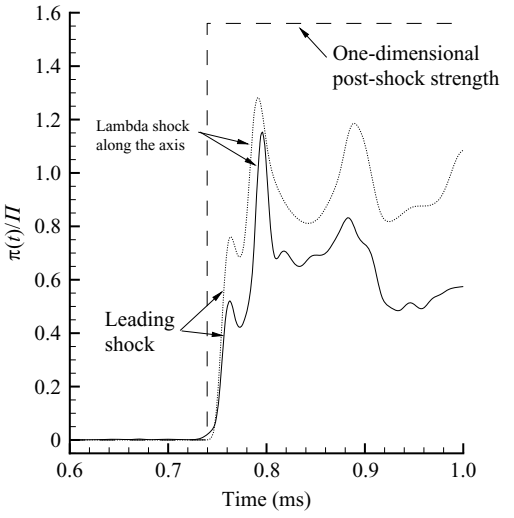

FIGURE 8. Enlarged view from figure 2(*a*). Measurements (–) against the numerical simulations (· · ·) and the one-dimensional results (— — —) corresponding to a complete opening.

the differences between the measured signals in figures 2 and 3 and the expected step signal, corresponding to a normal shock wave propagating along the tube as the result of an instantaneous and complete opening of the diaphragm. The first pressure peak is due to the arrival of the first shock front, that is followed by a system of rarefaction waves which alternate with reflected shocks. Therefore, the measured total pressure at the tube axis exhibits an oscillating profile around an average post-shock value, as discussed in §4.1. In figure 8, a detailed view of the signal in figure 2(*a*) is shown. With reference to figure 7, the first peak in the total pressure profile is due to the first shock wave, whose intensity is reduced with respect to the expected one-dimensional value owing to the interaction with the first rarefaction wave system centred at the diaphragm edge (see figure 4). The pressure is then reduced owing to the arrival of the portion of the rarefaction wave that has not yet coalesced into the first shock. Then, the pressure rises again owing to the arrival of the lambda shock at the tube axis. Further shock reflections, being of regular type and very weak, result in the pressure oscillations around the average post-shock total pressure Π. Therefore, the value of Π is determined by the contributions of the leading and axis lambda shocks only. It is remarkable that the aforementioned three-dimensional flow features are clearly visible along the shock tube axis (see figure 8) thus increasing the confidence in the representativity of the numerical simulations, that have been validated using total pressure measurements along the shock tube axis only.

A final commentary on the above results concerns the diaphragm opening time. In the case discussed above ($d/D = 0.6$), high-speed camera recordings give $\Delta t_{open} =$ 280 μs (see table 1), which is larger than the time levels $t = 43$, 65 and 195 μs shown in figures 4–6. However, as discussed at the beginning of the present section, the approximation of assuming an instantaneous opening of the diaphragm results in differences between numerical predictions and experimental observations that are limited to a time span that is comparable with Δt_{open}. In the next section, experimental observations far downstream of the diaphragm section are used to show that the complexity of the flow field close to the diaphragm, including the wave

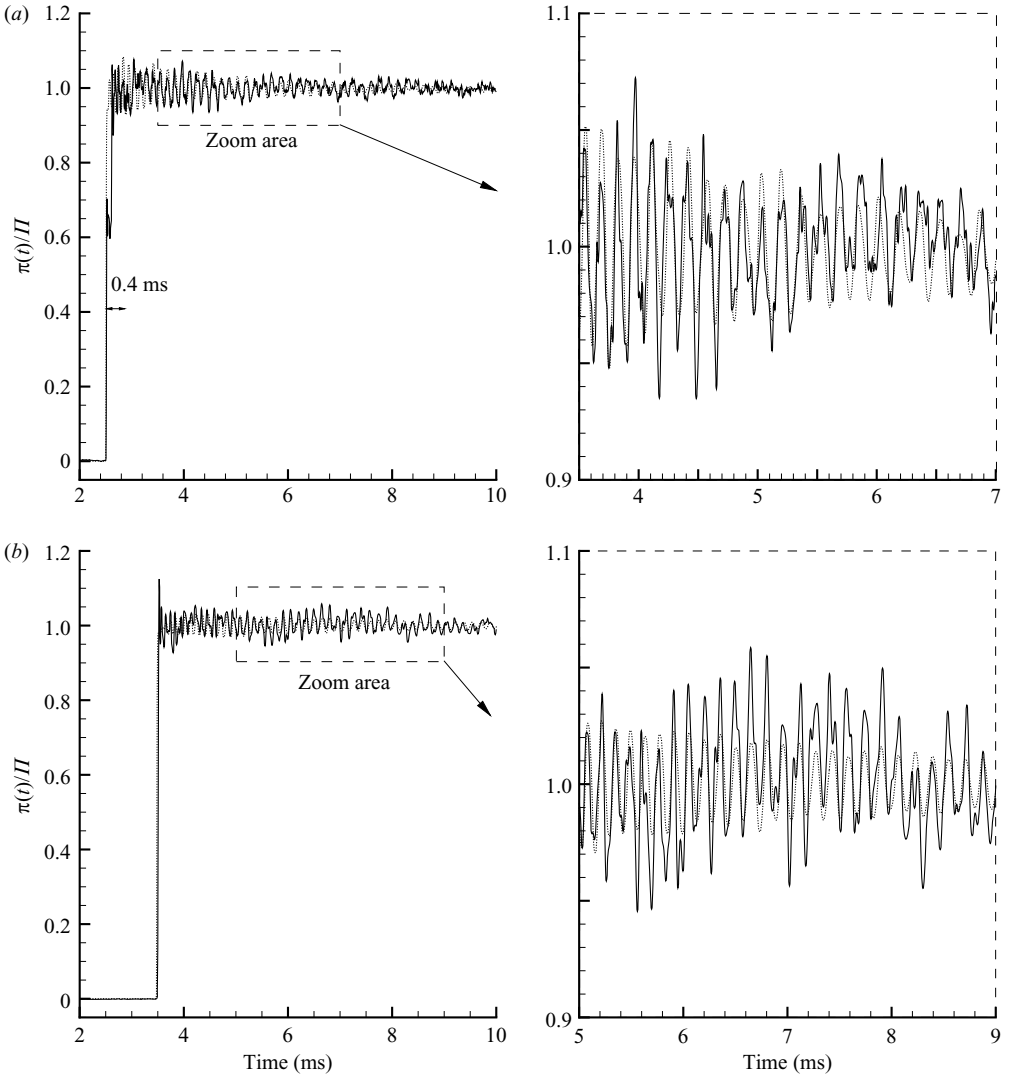

FIGURE 9. (*a*) Total pressure measurements (—) with $d/D = 0.7$ and $P_4/P_1 = 1.9$, against numerical simulations (···). The probe was located in the third position (970 mm, about $12D$ downwind of the diaphragm). (*b*) Probe located at the fourth position (1650 mm, about $20D$ downwind of the diaphragm).

reflection pattern and the diaphragm dynamics, is lost owing to the coalescence of the first waves into a single shock front.

4. Distant flow field features

The focus of the present section is to study the effects of the partial diaphragm burst at measurement stations sufficiently distant from the diaphragm itself. Figure 9 reports the experimental and numerical signals at two measurement stations located at $x/D = 12.125$ and 20.625, respectively. The pressure signal is characterized by an initial step, which heralds the arrival of a single shock front at the measurement station, followed by the pressure disturbances described in the previous section. The

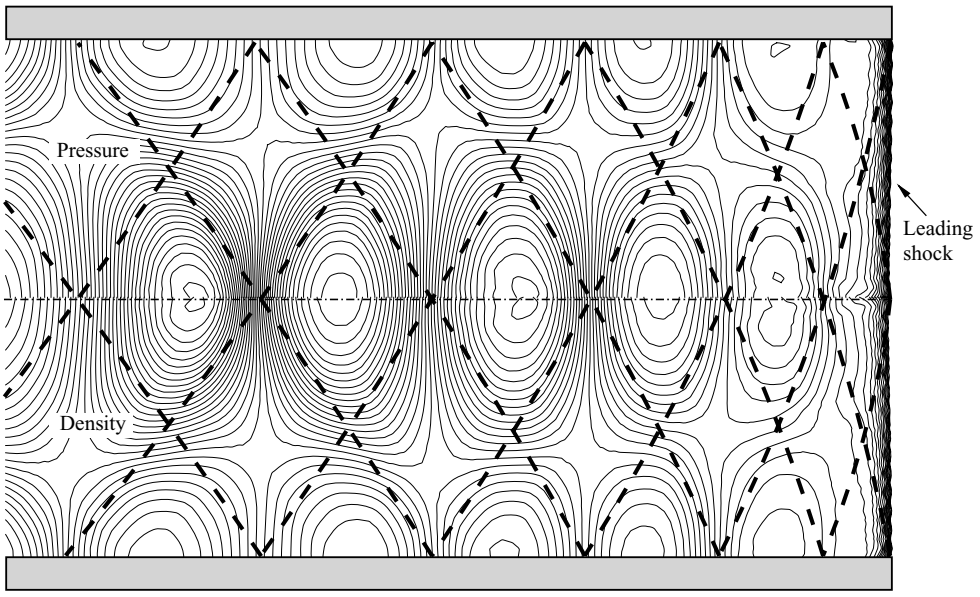

FIGURE 10. Computed representative flow field (isobars, top, and isopycnics, bottom) at time $t = 2.22$ ms in the region $8.75 < x/D < 10.6$, for $d/D = 0.7$. Dashed lines are added to identify the system of compression–rarefaction waves past the shock front.

total pressure oscillates around a post-shock value which is found to be constant in time and not to depend on the axial distance from the diaphragm, see §4.1.

The agreement between the experiments and the numerical simulations is very good in terms of both the post-shock pressure level and the local frequency of post-shock oscillations. The amplitude of the oscillations in the numerical signal is slightly lower than the experimental value in figure 9(*b*), possibly because of numerical damping which becomes more evident as the distance from the diaphragm increases.

In figure 10, pressure and density contours from simulations are shown in the region $8.75 < x/D < 10.6$. Sufficiently far from the diaphragm section, a single normal shock front is observed, that is followed by a system of rarefaction and compression waves that propagate as acoustic waves. The flow field is very simple if compared to that observed close to the diaphragm section. In the following, this regime will be referred to as the *distant flow field*.

The occurrence of such a simple flow field can be explained as follows. As it moves towards the low-pressure section of the shock tube, the diffracted portion of the shock wave (see figure 5) becomes planar and normal to the shock tube axis, similarly to what is observed in the propagation of a spherical wave, in which the local curvature of the wavefront decreases as the distance from its centre increases. An almost planar shock is therefore eventually formed; the small curvature of this wave accounts for the formation of the two systems of reflected compression/rarefactio waves shown in figure 10, that are symmetric with respect to the shock tube axis and generate the oscillatory (compressive-rarefactive) behaviour of the pressure signal measured by a stationary observer past the leading shock wave.

Remarkably enough, all details depending on the diaphragm opening dynamics are lost in the distant flow field. Owing to the higher temperature and flow velocity in the compressed gas, post-shock waves move faster than the leading shock and eventually coalesce into the single shock front depicted in figure 10. Therefore, the

assumption of considering an instantaneous diaphragm burst in the simulation does not introduce any relevant error in the prediction of the distant flow field. Therefore, we can conclude that in the distant flow field, deviations from the step signal expected from one-dimensional theory are limited to the strength of the leading shock, to be discussed in §4.1, and to the occurrence of post-shock oscillations, which are the subject of §4.2.

4.1. *Intensity of the leading shock wave*

The distant flow field is characterized by the occurrence of a normal shock front of constant strength whose intensity is significantly lower than that expected from the one-dimensional theory – corresponding to a complete and instantaneous opening of the diaphragm. The shock strength reduction results from the nonlinear interaction of the initial normal shock front with the complex wave field described in §3. In particular, with reference to figures 7 and 8, the post-shock pressure level is determined by the first compression–rarefaction wave system – resulting from the interaction of the initial shock wave with the rarefaction wave originated at the diaphragm edge (cf. figure 4) – and by the lambda shock at the axis of symmetry. As a consequence, an analytical estimation of the shock strength in the distant flow field is very difficult.

The analytical models of (Chisnell 1957; Alpher & White 1958; White 1958), and Nettleton (1973), which were devised to determine the shock attenuation in shock tubes with area change, were tentatively applied to the present case to compute the strength of the shock diffracting from the reduced diaphragm area $\pi d^2/4$ to the internal shock tube cross-sectional area $\pi D^2/4$. However, all these models significantly over-predict the reduction of the shock intensity measured in the present experiment. This is possibly due to the interaction with the corresponding diffraction process of the rarefaction wave propagating towards the high-pressure section. The cited models rely on a quasi-one-dimensional representation of the flow whose analytical solution is obtained via characteristic reconstruction in simple wave regions. In the present problem, the rarefaction wave centred at the diaphragm edge, that is generated by the diffraction of the leading shock, interacts with the corresponding compression wave on the high-pressure side of the diaphragm. This results in non-simple wave regions even in the quasi-one-dimensional approximation, thus making the development of an analytical tool unfeasible.

To provide a quantitative measure of the shock intensity, a non-dimensional shock strength Π/Π_{1D} was considered, where Π_{1D} is the one-dimensional shock strength. Experimental and numerical results are reported in figure 11, where the simple correlation

$$\frac{\Pi - \Pi_{1D}}{\Pi_{1D}} = \left(1 - \left(\frac{d}{D}\right)^2\right)^3 \tag{4.1}$$

is also shown. The functional form (4.1) has been devised from dimensional considerations; the shock intensity is assumed to depend only on the ratio of the area of the opened portion of the diaphragm $a = \pi d^2/4$ to the internal shock tube cross-sectional area $A = \pi D^2/4$. The very good agreement between numerical and experimental results in figure 11 supports this hypothesis and confirms that the diaphragm dynamics play a negligible role in shock attenuation. A simple power law in the form $(\Pi - \Pi_{1D})/\Pi_{1D} = (1 - a/A)^\alpha$ was therefore considered; $\alpha = 3$ in (4.1) provides the best fit to experimental and numerical data. Note that $\Pi = \Pi_{1D}$ for $d = D$, that is, for a complete opening, and that $\Pi = 0$ for $d = 0$.

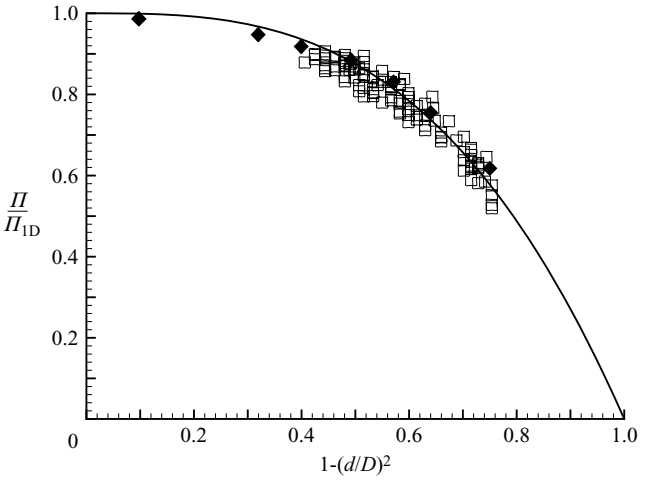

FIGURE 11. Reduction of shock strength as a function of the diaphragm opening section. Experimental results (□), simulations (◆) and correlation (4.1) (—).

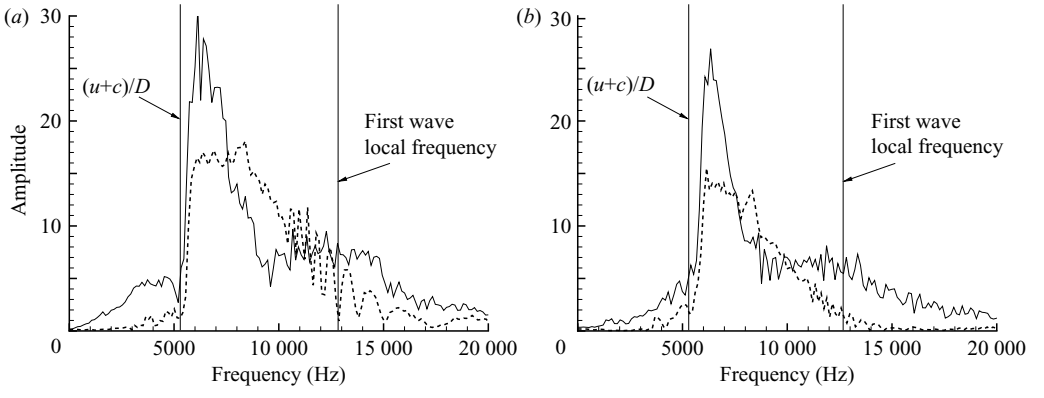

FIGURE 12. (*a*) Fourier transform of total pressure signal at measurement station $x = 0.97$ m ($x/D = 12$): experimental (—) and numerical (···) results for $d = 56$ mm ($d/D = 0.7$) in the (ideally constant) post-shock region. The limiting frequencies $f_\infty = (u + c)/D$ and the local frequency of the first wave are also indicated. (*b*) Fourier transform of total pressure signal at measurement station $x = 1.65$ m ($x/D = 20$).

4.2. *Post-shock pressure disturbances*

In this section, post-shock pressure disturbances are studied. To this purpose, a simple model for the generation and the propagation of the pressure oscillation is proposed and verified against the numerical and experimental results. The dependence of the amplitude of the pressure fluctuations on the axial coordinate and on the relative area of the opened portion of the diaphragm is also investigated.

4.2.1. *A simplified model for shock propagation*

Further inspection of the instantaneous pressure and density fields in figure 10 reveals that the spatial separation between two successive compression or rarefaction waves increases with the distance from the leading shock. At a given measurement location, this results in a reduction of the local wave frequency of the pressure oscillations past the shock wave. Therefore, in the frequency domain, the measured

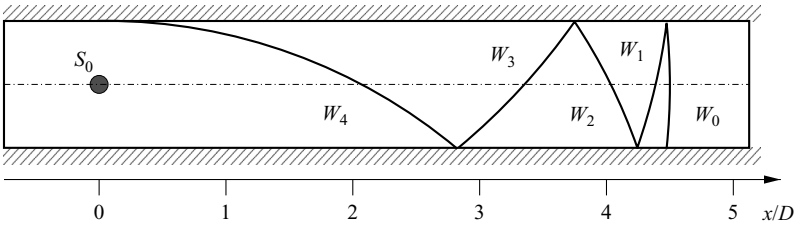

FIGURE 13. Wave reflection scheme at intermediate distance from the diaphragm.

pressure signal is characterized by a wide spectrum of disturbances with respect to the theoretical step profile, which in our experiments ranges from about 5 kHz to about 15 kHz. This can be appreciated in figure 12, where the amplitude spectra of the pressure signal past the leading shock are shown for $x/D = 12$ and 20.

To explain the dependence of the local frequency on time and on the axial coordinate of the measurement station, a simplified model for wave propagation is now introduced. In the model, the leading shock wave W_0 is represented by a spherical wave propagating at speed σ_0 from the origin S_0, which is located along the tube axis at the diaphragm section. The first wave reflection at the tube walls is accounted for by introducing a suitable image spherical wave W_1 centred at point S_1, which is located at a radial distance D from S_0. The jth reflection is then accounted for by introducing the corresponding image wave W_j, centred at point S_j located at a radial coordinate $(-1)^j\, jD$, and moving at speed σ_j, which is assumed here to be equal to the acoustic wave speed $u + c$, with u and c post-shock values of the flow velocity and speed of sound, respectively. Figure 13 depicts the wave system obtained from the model after four reflections, to be confronted with the distant flow field in figure 10.

The time of arrival of the jth reflected wave at point P located at distance L from S_0 is therefore

$$t_j = \frac{R_j}{c} = \frac{L}{(u+c)\sin\alpha_j},$$

where $\alpha_j = \arctan(L/jD)$. As L increases, the curvature of the leading wave reduces, in accordance with the numerical observations. From the expressions above, the local frequency f_j can be computed as the inverse of the time span between two successive waves, namely, $f_j = 1/(t_{j+1} - t_j)$. Simple calculations show that

$$f_\infty = \lim_{j\to\infty} f_j = \frac{u+c}{D}.$$

The frequency f_∞ is the limiting local frequency of the pressure perturbations and it is indicated in figure 12, where the local frequency of the first post-shock wave f_{max} is also shown. The local frequencies of the post-shock disturbances – obtained either experimentally or numerically – are found to be bounded by these two limiting frequencies. The local frequency of the jth wave is computed from the model as

$$f_j = \frac{f_\infty}{2j+1}\left[\sqrt{(j+1)^2 + l^2} + \sqrt{j^2 + l^2}\right] = f_\infty \phi(j, l),$$

where $l = L/D$ is the dimensionless distance from the diaphragm. The local frequency f_j depends only on the limiting frequency f_∞ and on the axial position. To account for the coalescence of $j > 0$ waves into the leading shock W_0, the propagation velocity σ_0 is taken as the measured shock speed, whereas the wave speed σ_j for $j > 0$ is the

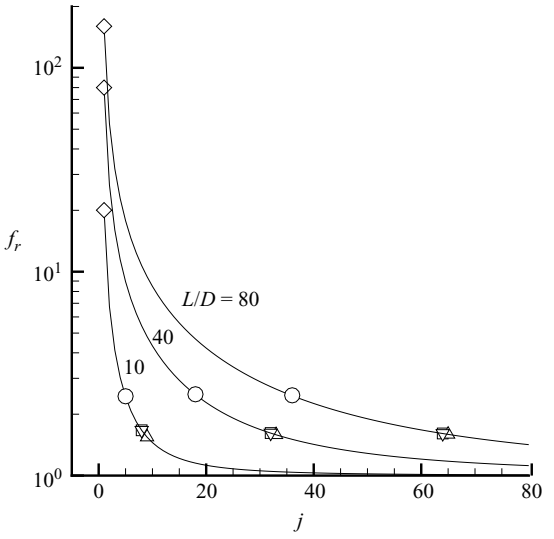

FIGURE 14. Local frequency $f_r = f/f_\infty$ of post-shock waves as a function of the wavenumber j for different axial positions. The limiting wavenumbers j_{min} are indicated for the wave Mach numbers $M_{W_0} = 1$ ($\diamond$), 1.12 ($\bigcirc$, nominal conditions), 2 ($\triangledown$), 3 ($\triangle$) and 6 ($\square$).

acoustic wave speed $u + c$, as discussed above. All waves for which $t_j < t_0 = L/\sigma_0$ are therefore neglected, since they correspond to waves that coalesced into the shock front. The limiting value j_{min}, such that $t_{j_{min}+1} \geqslant t_0$, of the first wave is therefore easily obtained as

$$j_{min} = 1 + l\sqrt{\left(\frac{u+c}{\sigma_0}\right)^2 - 1},$$

and corresponds to the maximum local frequency past the leading shock, f_{max}. Note that the value of j_{min} depends on the axial coordinate l as well as on the values u, c and σ_0, which in turn depend only on the pressure ratio P_4/P_1 or, equivalently, on the shock Mach number $M_{W_0} = \sigma_0/c_1$. In figure 14, the reduced local frequency $f_r = f/f_\infty$ of post-shock waves is reported as a function of the wavenumber j. Curves are parameterized with the axial positions L/D. These curves are independent of the leading shock Mach number, which influences only the value of j_{min} that is indicated along each curve for different values of M_{W_0}.

For all the axial positions, the local frequency is found to decrease with increasing j or, equivalently, in time, see figure 13. For a given wavenumber j, the local frequency increases with the distance from the diaphragm section. Indeed, the radius of curvature of the waves increases with L and hence the spatial separation between two waves decreases, as in figure 13, thus resulting in an increase of the local frequency. For a given shock Mach number M_{W_0}, the maximum reduced frequency is found to be almost independent of the axial coordinate l, but for the case $M_{W_0} = 1$. At high wave Mach numbers, it is also independent of M_{W_0} and equal to about 1.6. On the contrary, the value of j_{min} strongly depends on l and shows almost no dependence on the wave Mach number for $M_{W_0} > 2$.

The dependence of the local frequency on time cannot be appreciated in figure 14, which is obtained by a Fourier analysis of the whole experimental and numerical signal. In figure 15, time-frequency analyses of the pressure signal at different

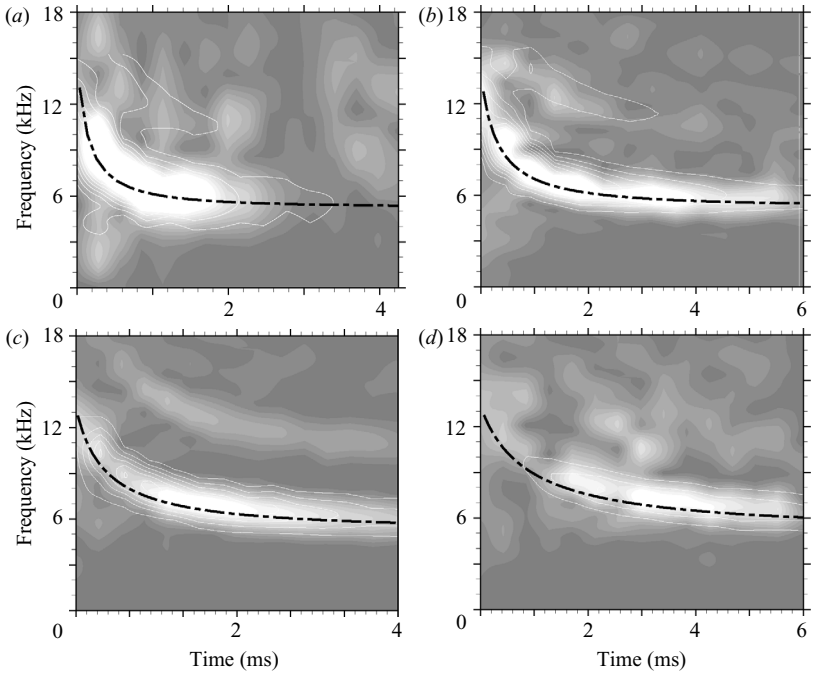

FIGURE 15. Time-frequency analysis of the post shock plateau for stations (*a*) $x/D = 6$, (*b*) $x/D = 12$, (*c*) $x/D = 20$ and (*d*) $x/D = 35$. $d/D = 0.7$.Isolines of the amplitude of the pressure signal for experimental (B/W field) and numerical (white isolines) data. Results from the analytical model are represented with a line (– · –), since the model does not give any amplitude indication.

measurement stations is reported.In the plots, results from the proposed model are also drawn.The time span for the calculation of the amplitude spectra is 875 μs, a value which includes the overlap between adjacent intervals(50%). The proposed model predicts fairly well the local frequency corresponding to the maximum amplitude of post-shock oscillations. Unfortunately it does not provide any indication of the intensity of pressure disturbances, since it is based on the acoustic theory. Nevertheless, experimental and numerical results in figure 15 indicate that the average amplitude of the oscillations is decreasing with the axial position, as discussed in the next section.

4.3. *Amplitude of the post-shock oscillations*

To provide a quantitative measure of the amplitude of post-shock pressure disturbances at different measurement stations and for different opening diameters, the mean harmonic energy (MHE) introduced by Persico *et al.* (2005) is used here. The MHE is defined as follows

$$\mathrm{MHE} = \frac{1}{N_\mathrm{f}} \sum_{k=k_1}^{k_2} \sum_{n=0}^{N_\mathrm{p}-1} \left[\frac{\pi(t)}{\Pi} - 1 \right] \exp^{(-2\pi \mathrm{i} \frac{kn}{N_\mathrm{p}})}, \tag{4.2}$$

and it is proportional to the energy content of the pressure perturbations in the frequency range of interest, which from experiments and simulations is about 4–15 kHz (see figure 12). The average elapsed time between the leading shock and the arrival of the reflected expansion wave is $\hat{t} = 7.4$ ms; accordingly, a frequency

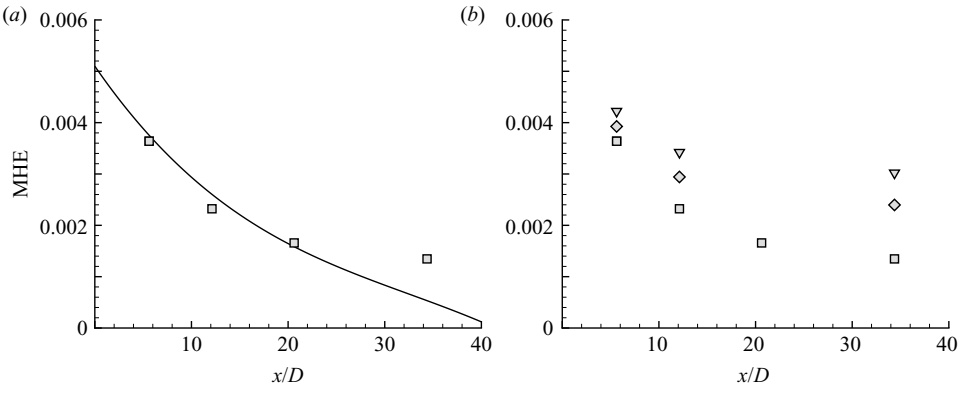

FIGURE 16. (*a*) MHE as a function of the axial distance from the diaphragm section for $d/D = 0.7$. Experimental (□) and numerical (—) results. (*b*) Experimental results for $d/D = 0.5$ (▽), $d/D = 0.6$ (◇), $d/D = 0.7$ (□).

resolution $\Delta f = 1/\hat{t}$ of 135 Hz is used. The MHE is computed from the lowest frequency of $f_1 = k_1 \Delta f = 4.05$ kHz ($k_1 = 30$) to $f_2 = k_2 \Delta f = 14.985$ kHz ($k_2 = 111$). If the shock is not completely formed at the considered measurement stations, a high-pass filter is used to remove the transient portion of the signal corresponding to the pressure shock from P_1 to $\overline{P^t}$. In the definition (4.2), $N_f = k_2 - k_1 = 81$ and the number of sample points is $N_p = f_s \hat{t} = 7400$, with $f_s = 1$ MHz sampling frequency.

In figure 16(*a*), the computed and measured values of MHE in the nominal configuration are reported for all five axial distances considered in the experiments. Five to ten experimental runs were used to evaluate the average value of the MHE at a given measurement station. The experimental and numerical results are significantly different only at distances higher than $x/D = 20$, where the numerical dissipation of the scheme is larger owing to the use of a coarser grid far from the diaphragm.

The amplitude of pressure oscillations decreases as the distance from the diaphragm increases. A large decrease of the value of the MHE is observed for $3 < x/D < 10$, where the first (strong) shock reflections start coalescing into the leading shock. The rate of reduction is significantly lower between $x/D = 10$ and $x/D = 40$, where the main source of attenuation is viscous damping. Note that the larger amplitudes are concentrated into the highest frequencies – which corresponds to perturbations immediately following the leading shock – at measurement stations close to the diaphragm (see figure 9(*a*)). On the contrary, the amplitude is almost constant for all frequencies at larger distances (figure 9(*b*)). The above can be appreciated more clearly in the time-frequency plots in figure 15.

In figure 16(*b*), the influence of the opening diameter d/D on the value of the MHE is reported. The value of MHE at each measurement station is observed to increase as the opening portion of the diaphragm is reduced. Indeed the portion of the shock wave that is diffracted at the diaphragm edge – which accounts for the formation of post-shock disturbances, see figure 4 – decreases with d/D and tends to zero as d/D tends to 1. In the cases $d/D = 0.5$ and $d/D = 0.6$, viscous damping is no more negligible, in particular in determining the dynamics of the slip line, and the inviscid-flow simulations are no longer suitable for describing the flow physics.

5. Conclusions

Experimental and numerical studies were carried out to investigate the flow field resulting from the incomplete burst of a shock tube diaphragm. The partial opening of the diaphragm causes the reduction of the shock intensity and the appearance of post-shock pressure oscillations.

Close to the diaphragm section, a complex wave field is generated as the leading shock wave diffracts from the diaphragm orifice. The diffracted portion of the shock is reflected at the tube walls and interacts with the annular vortex shedding from the diaphragm edge. A system of compression and rarefaction waves is formed, thus resulting in pressure oscillations past the leading shock.

Sufficiently far from the diaphragm, a single shock front is formed and reflected shocks and rarefaction waves simplify to acoustic disturbances whose local frequency has been studied by means of an analytical model. The resulting flow field is found to be independent from the peculiarities of the diaphragm dynamics, since all initial perturbations eventually coalesce into the leading shock wave. The local frequency of the pressure oscillations is found to decrease in time at a given distance from the diaphragm and to increase with the distance from the diaphragm. The lowest limiting frequency is found to be independent of the axial coordinate and to be approximatively equal to the ratio of the acoustic speed $u + c$ in the post-shock region to the shock tube diameter. The highest limiting frequency depends instead on the axial coordinate and on the wave Mach number. The amplitude of post-shock pressure oscillation is found to decrease as the distance from the diaphragm is increased, and to be inversely proportional to the diameter of the opening section of the diaphragm.

REFERENCES

Ainsworth, R. W. & Allen, J. L. 1990 Investigating the performance of miniature semi-conductor pressure transducers for use in fast response aerodynamic probes. In *Proc. 10th Symp. Meas. Tech. Turbomachines*.

Alpher, R. A. & White, D. R. 1958 Flow in shock tube with area change at the diaphragm section. *J. Fluid Mech.* **3**, 457–470.

Barkhudarov, E. M., Mdivnishvili, M. O., Sokolovp, I. V., Taktakishvili, M. I. & Terekhin, V. E. 1991 Mach reflection of a ring shock wave from the axis of symmetry. *J. Fluid Mech.* **226**, 497–509.

Chisnell, R. F. 1957 The motion of a shock wave in a channel, with applications to cylindrical and spherical shock waves. *J. Fluid Mech.* **2**, 286–298.

Fergason, S. H., Guardone, A. & Argrow, B. M. 2003 Construction and validation of a dense gas shock tube. *J. Thermophys. Heat Transer* **17** (3), 326–333.

Gaydon, A. G. & Hurle, I. R. 1963 *The shock tube in high temperature chemical physics*. Reinhold.

Glass, I. I. & Sislian, J. P. 1994 *Nonstationary Flows and Shock Waves*. Clarendon.

Gossweiler, C., Humm, H. J. & Kupferschmied, P. 1990 The use of piezo resistive semi-conductor pressure transducer for fast-response probe measurements in turbomachinery. In *Proc. 10th Symp. Meas. Tech. Turbomachines*.

Guardone, A. 2007 Three-dimensional shock tube flows of dense gases. *J. Fluid Mech.* **583**, 423–442.

Guardone, A. & Vigevano, L. 2007 Finite element/volume solution to axisymmetric conservation laws. *J. Comput. Phys.* **224**, 489–518.

Hickman, R. S., Farrar, L. C. & Kyser, J. B. 1975 Behavior of burst diaphragms in shock tubes. *Phys. Fluids* **18** (10), 1249–1252.

Mirels, H. 1963 Test time in low-pressure shock tubes. *Phys. Fluids* **6** (9), 1201–1214.

Mirels, H. & Mullen, J. F. 1964 Small perturbation theory for shock-tube attenuation and nonuniformity. *Phys. Fluids* **7** (8), 1208–1218.

Nettleton, M. A. 1973 Shock attenuation in a 'gradual' area expansion. *J. Fluid Mech.* **60**, 209–223.

Paniagua, G. & Dénos, R. 2002 Digital compensation of pressure sensors in time domain. *Exps. Fluids* **32**, 417–424.

Persico, G., Gaetani, P. & Guardone, A. 2005 Dynamic calibration of fast-response probes in low-pressure shock tubes. *Meas. Sci. Technol.* **16**, 1751–1759.

Petrie-Repar, P. & Jacobs, P. A. 1998 A computational study of shock speeds in high-performance shock tubes. *Shock Waves* **8**, 79–91.

Rothkopf, E. M. & Low, W. 1974 Diaphragm opening process in shock tubes. *Phys. Fluids* **17** (6), 1169–1173.

Sun, M. & Takayama, K. 2003 Vorticity production in shock diffraction. *J. Fluid Mech.* **478**, 237–256.

White, D. R. 1958 Influence of diaphragm opening time on shock-tube flows. *J. Fluid Mech.* **4**, 585–599.